

On the dissipated energy density in compression

*Original*

On the dissipated energy density in compression / Ferro, GIUSEPPE ANDREA. - In: ENGINEERING FRACTURE MECHANICS. - ISSN 0013-7944. - 73:(2006), pp. 1510-1530.

*Availability:*

This version is available at: 11583/1400313 since:

*Publisher:*

*Published*

DOI:

*Terms of use:*

This article is made available under terms and conditions as specified in the corresponding bibliographic description in the repository

*Publisher copyright*

(Article begins on next page)



# On dissipated energy density in compression for concrete

Giuseppe Ferro \*

*Politecnico di Torino, Department of Structural Engineering and Geotechnics, Corso Duca degli Abruzzi 24, I-10129 Torino, Italy*

Received 29 August 2005; received in revised form 17 January 2006; accepted 24 January 2006

## Abstract

An experimental investigation on drilled cylindrical concrete specimens in compression over a large scale range (1:19) has been carried out to evaluate the variation of some mechanical parameters by varying specimen size. The peculiarity of the present investigation consists in exploring very small specimen dimensions. The experimental results show scale effects on dissipated energy density rather than on uniaxial compressive strength. A theoretical explanation for such a phenomenon, based on fractal hypothesis, is presented and a comparison between experimental and theoretical values is discussed. © 2006 Elsevier Ltd. All rights reserved.

**Keywords:** Fracture mechanisms; Powder compaction; Concrete; Structures; Mechanical testing

## 1. Introduction

The advent of computers has considerably changed the capabilities in design and analysis of concrete structures. The extensive use of powerful computers and finite element codes in structural analysis is meaningful only if suitable and reliable constitutive laws for the material are available. In design, however, concrete is generally classified on the basis of its compressive strength. A correct evaluation is therefore fundamental.

In general, the constitutive relations and the mechanical parameters for concrete are obtained from standard specimens. The sizes and shapes of compressive strength test specimens of concrete vary from one country to another. Commonly used standard sizes are 150 mm for cubes and 150 × 300 mm for cylinders. The introduction of high-strength concrete, with compression strength up to five times the standard strength, suggests the use of smaller specimens, with the advantages of maintaining the standard test machines available in the laboratories, easy handling, and using less concrete. Another important application of reducing specimen sizes is constituted by the determination of the concrete strength for existing structures by drilling small specimens. This technique is very useful, the deterioration of the mechanical properties for concrete structures being one of the main problems in civil engineering.

The choice of the standard size is affected by the variation of the compressive strength with size and height/diameter (or slenderness) ratio. This variation is high when the rigid test machine platens are in direct contact

\* Tel.: +39 11 5644885; fax: +39 11 5644899.

E-mail address: [ferro@polito.it](mailto:ferro@polito.it)

### Nomenclature

$\delta$	displacements
$\epsilon$	strain
$\epsilon_{\text{peak}}$	strain at the peak stress
$d$	specimen diameter
$h$	specimen height chosen as the characteristic specimen size
$\epsilon_m$	mean deformation
$f'_c$	compression strength
C1	smallest specimen set with $h = 10$ mm
C2	specimen set with $h = 23$ mm
C3	specimen set with $h = 46$ mm
C4	specimen set with $h = 100$ mm
C5	largest specimen set with $h = 190$ mm
C33	third specimen of the set with $h = 46$ mm
$N$	number of fragments in fragmentation process
$r$	characteristic linear dimension of fragments
$B$	constant of proportionality
$D$	fractal dimension of the fragmentation process
$V_f$	total volume (mass) of fragments
$r_{\text{max}}$	characteristic linear dimension of the largest fragment
$r_{\text{min}}$	characteristic linear dimension of the smallest fragment
$k$	constant of proportionality
$V$	volume of the un-fragmented specimen
$A_f$	total surface area of the fragments
$C$	geometrical factor depending upon the average shape of the fragments
$W$	energy dissipated to produce a new free surface in the fragmentation process
$\beta_F$	specific energy absorbing capacity;
$\mathcal{G}$	elastic energy release rate or specific energy necessary to generate the unit area of fracture
$d_\omega$	fractal dimension of the fragmented set = 3-D
$h^*$	measure of the fractal set representing the fragmented configuration
$S$	dissipated energy density
$\mathcal{G}_F^*$	fractal dissipated energy density parameter
$\epsilon^*$	renormalized fractal strain
$E^*$	renormalized fractal elastic modulus

32 with the concrete specimen, the lateral deformation of concrete being restrained at the specimen ends. A wide  
 33 investigation has been carried out by Carpinteri et al. [1].

34 Very interesting results have been obtained in a round robin test organized by the RILEM Committee  
 35 148 SSC “Strain-Softening of Concrete” [2], whose aim was to investigate the softening behavior of concrete  
 36 by varying specimen dimensions, boundary conditions, feed-back signals and testing machine characteris-  
 37 tics. They observed the independence of the slenderness (or size) on the compressive strength, when the  
 38 boundary conditions of the concrete specimens were characterized by no friction (or reduced friction) at  
 39 the ends.

40 The effect of size on the mechanical properties of concrete is also important when small scale models are  
 41 used to predict the behavior of real structures. Early work on the size effect in compression dates back to  
 42 the 1920s. Gonnermann [3] emphasized the size effects through an extensive investigation on the compressive  
 43 strength of cylinders with a height/diameter ratio equal to two.

44 Many other authors fronted the problem of size effects on nominal strength for concrete in compression.  
 45 Blanks and McNamara [4] performed tests on cylindrical specimens with slenderness of  $h/d = 2$  in a large scale

range (1:12), while Jishan and Xixi [5] performed experiments on cubes (scale range 1:4) and on prisms with  $h/d = 3$  (scale range 1:3). Other analyses on size effects in compression were conducted by considering particular geometries, as compact compression tests [6], reinforced concrete columns [7] and high-strength concrete reinforced with randomly distributed fibers [8]. Several assessments were made on the size effects through the extensive experimental work reported in the literature [9].

The nominal compressive strength is obtained by dividing the peak force by the initial specimen cross-section area. This operation has the meaning of estimating a global material property, ignoring at the same time the material structure as well as the material failure behavior during the test. Momber [10] analyzed the fragmentation of standard concrete cylinders under compression. He observed that the standard codes (ASTM C39-86) consider types of failure which involve only large primary fracture debris, while after compression testing of any concrete specimen, fragments of fine-grained material are generated. Slate and Hover [11] showed pervasive internal crack growth up to the peak load by studying the interior of concrete specimens that were loaded up to a certain level and that were subsequently unloaded. From their experimental observations, it is believed that energy dissipation in the pre-peak regime is a global continuum-dominated process that may be attributed to microcracking throughout the entire specimen. On the other hand, energy dissipation in the post-peak regime is a localized surface-dominated fracture process after the coalescence of microcracks in the peak regime. Vardoulakis et al. [12] proposed a continuum fracture mechanics of uniaxial compression on brittle materials to arrive at a continuum description of the observed post-peak phenomena. Their conclusions, based on experimental evidence and dimensional analysis, state that the post-peak axial stress is a function of the axial displacement normalized by the radius of the specimen, and not by its height. Van Vliet and van Mier [13], observed that post-peak data from uniaxial compression experiments on plain concrete suggest a stress–displacement rather than a stress–strain relation.

An extensive experimental investigation on geometrically similar cylindrical concrete specimens in compression obtained by a unique concrete block is herein presented to evaluate the variation of some mechanical parameters by varying specimen size on a very large scale range (1:19) and by avoiding frictional restraint between the loading platens and the specimen. The peculiarity of the present investigation consists in exploring very small specimen dimensions. One of the main goals of the present paper is the measure of the energy dissipated in destroying or fragmenting a volume of concrete.

From a phenomenological point of view, the softening branch of the load–displacement curve is governed by macrocracking, after the coalescence of the initial microcracks. As shown by the experimental results, the ultimate compressive strength of concrete depends on the type of testing machine, the specimen size and the nature of the contact between the machine platens and the specimen. In this paper, it is shown how, avoiding friction, the strength is almost independent of specimen dimension, whereas strong variations are observed for dissipated energy density in compression. A theoretical explanation, recently proposed by Carpinteri and Pugno [14,15], for the scale effects on the dissipated energy density in compression is discussed and applied to the experimental results. This is based on the concept of fractal geometry [16,17], and on the fragmentation approach [18]. From the theory, it can be shown how, in the scale range of the tested specimens, the energy dissipation is a surface-dominated phenomenon and damage localization occurs in small concentrated zones. This statement is valid only for small specimen sizes, while for larger structural dimensions the energy dissipation should be a volume-dominated process and damage is more spatially distributed.

## 2. Experimental set-up

The ambition of testing concrete specimens in compression in a very wide size range strongly impacts with the laboratory set-ups, which opposes physical limits. The fundamental idea was to use a very simple standard testing apparatus composed only of a closed-loop servo-hydraulic system and strain gauges glued on the specimen to record the longitudinal as well as the transverse deformation in the pre-peak part of the force versus displacement curve. As the specimens were very different in size, two different set-ups have been adopted, even if this could cause some inconveniences due to different stiffnesses of the frames.

## 94 2.1. Test specimens

95 The first problem was that of defining the size and the slenderness of the test specimens. The size is limited by  
96 the dimension of the aggregates (lower limit) and by the potentialities of the available equipment (upper limit).

97 All the cylinders were obtained by drilling from a unique concrete block with sizes  $800 \times 500 \times 200$  mm. The  
98 microconcrete used for the specimens is characterized by a maximum aggregate size of 4 mm. The porosity is  
99 equal to 17.7 vol% and the distribution of pores is 15.8%  $> 10000$  nm, 52.9% 30–10000 nm and  
100 31.3%  $< 30$  nm. The nominal strength is  $51.8 \text{ N/mm}^2$  while the compression strength  $f'_c$ , obtained from cubes  
101 ( $150 \times 150 \times 150$  mm) after 28 days, is equal to  $33 \text{ N/mm}^2$ . The water–cement ratio is equal to 0.65.

102 Five different diameters were considered in relation to the disposable drilling core-bits in a scale range of  
103 1:19. The specimens were cylinders with a height/diameter ratio  $h/d = 1$  and  $h$  chosen as the characteristic  
104 dimension equal to 10, 23, 45, 100, 190 mm, respectively. Four specimens have been tested at each size.  
105 Two extra specimens for  $h = 10, 23$  and 45 mm were used to check the electrical parameters (impedance, gain).  
106 The geometries of the tested specimens are presented in Fig. 1a, while an overview of all the specimen sizes is  
107 reported in Fig. 1b. The geometrical characteristics are reported in Table 1.

## 108 2.2. Testing equipment

109 For the three smallest sizes, the tests were carried out on a uniaxial compression machine with a capacity of  
110 100 kN. The machine is controlled by a closed-loop servo-hydraulic system. Of the two loading platens, the  
111 lower is fixed, while the upper is connected to the machine hinge. In this way, the upper platen can adjust to  
112 the geometrical imperfections of the specimen. All compression tests with this machine have been performed  
113 under displacement control, by imposing a constant rate of the displacement of the upper loading platen.  
114 The displacement rate has been set in order to impose the same stress rate for all the specimen sizes. A stress  
115 rate equal to  $0.5 \text{ N/mm}^2/\text{s}$  was adopted, as prescribed by UNI Standard 6130 for cubic strength evaluation.  
116 To obtain this stress rate, the displacement rates have been set equal to  $2 \times 10^{-3} \text{ mm/s}$  for the smallest specimens  
117 ( $h = 10$  mm, C1),  $4.6 \times 10^{-3} \text{ mm/s}$  for the specimens with  $h = 23$  mm (C2) and  $10 \times 10^{-2} \text{ mm/s}$  for  $h = 46$  mm  
118 (C3). On each specimen two bidirectional strain gauges were glued, the length of which was taken proportional  
119 to the specimen height. More specifically, the strain gauge length was 1.5 mm for  $h = 10$  mm (strain gauge HBM  
120 1.5/120 xy 11), 3 mm for  $h = 23$  mm (strain gauge HBM 3/120 xy 11) and 6 mm for  $h = 45$  mm (strain gauge  
121 HBM 6/120 xy 11). The axial deformations as well as the lateral deformations in the middle part of the specimen  
122 were measured with these strain gauges, and the volumetric variation in the pre-peak part was determined. A  
123 detail of the three smallest specimens with the glued strain gauges is reported in Fig. 1c.

124 For the two remaining specimen sizes,  $h = 100$  (C4) and 190 mm (C5), a manual load-controlled uniaxial  
125 compression machine with a capacity of 3000 kN was used. The choice of this kind of machine was chosen for  
126 the following reasons. First of all, the height of the specimens do not permit control of the post-peak  $\sigma$ – $\epsilon$   
127 diagram under displacement control, due to the more brittle structural behavior. This aspect could be  
128 overpassed if the tests were controlled over a central part of the specimens, as performed by van Vliet and  
129 van Mier [19], or through lateral deformations [20]. The latter would have comported a very sophisticated test,  
130 which was not the author's intention. Secondly, the control of the explosive behavior of the specimens and the  
131 determination of the fragment sizes pushed the author toward the aforementioned solution. For these two  
132 larger sizes, loading cycles around the peak-load (characterized by a decrease of the slope in the load versus  
133 displacement diagram) were performed in order to capture the post-peak branch and to plot the entire curve.  
134 Unfortunately, as should have been easy to predict, only for one specimen (C44) it was possible to capture the  
135 softening part. On the other hand, two specimens (C41 and C42) were tested in displacement control with a  
136 different closed-loop servo-hydraulic machine with a capacity of 1000 kN. The stiffness of this machine was  
137 not enough and an explosive failure occurred.

## 138 2.3. Boundary conditions

139 In uniaxial compression tests it is well-known how the boundary conditions play an important role. When  
140 a concrete specimen is loaded between rigid loading platens (steel), the lateral deformation of concrete is

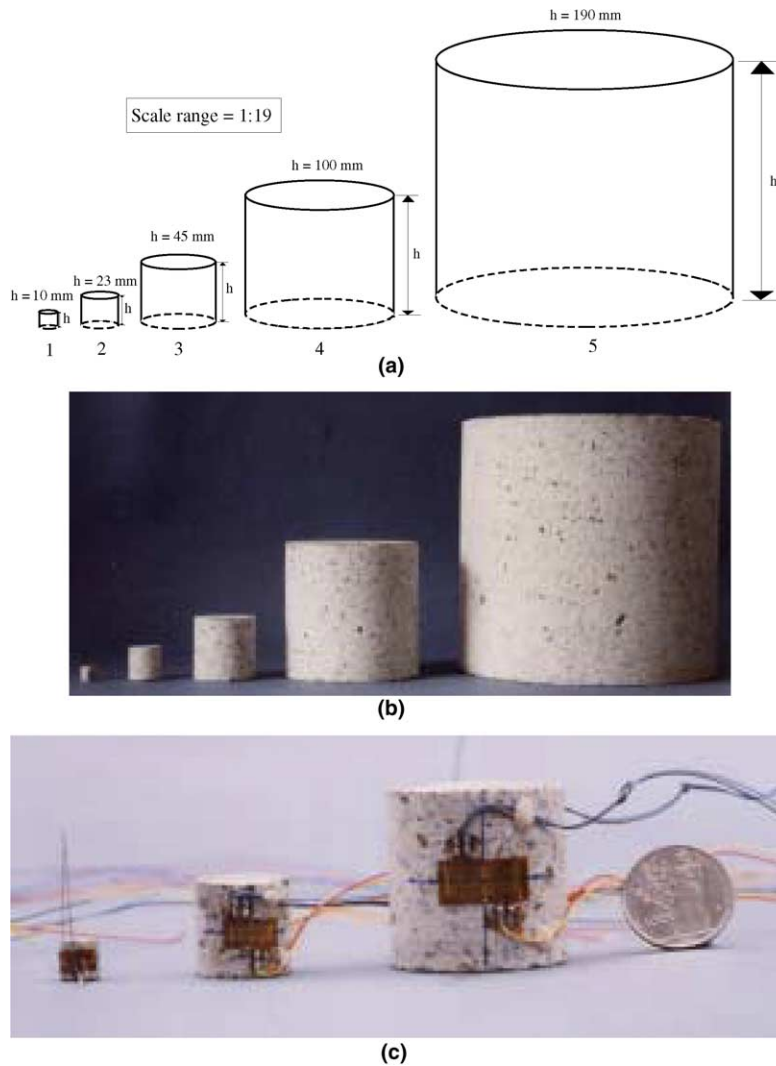


Fig. 1. (a) Geometry of the five different concrete specimens; (b) overall view of the five specimen sizes; (c) particular of the three smallest specimens with the glued strain gauges.

confined to the specimen ends (Fig. 2a), which are forced to have the same lateral deformation as the rigid platens. In this case, shear-stresses develop between specimen and loading platen, causing a three-dimensional state of stress at the specimen ends.

An opposite trend comes out when loading platens with a low stiffness and a high Poisson's ratio are used (rubber or brushes) (Fig. 2b). The platens are subjected to large lateral deformations and outward-directed shear forces develop at the interfaces, producing local splitting cracks.

Kotsovos [21] performed experiments on cylinders with an aspect ratio of 2.5 and with different frictional systems. He observed the same pre-peak behavior (in dimensionless form) for the different choices of loading system, and post-peak dimensionless stress-displacement curves characterized by increasing slope with decreasing the coefficient of friction. In order to minimize the interface friction, van Mier [22] and Vonk [23] developed brush platens. Wittmann et al. [24] tested normal-strength concrete cylinders by attaching at the ends two high-strength concrete disks of the same diameter. This system was also adopted by Lee and Willam [25].

Table 1  
Summary of geometrical characteristics of specimens

Specimen no.	Diameter (mm)	High (mm)	$A$ (mm <sup>2</sup> )	Weight (g)	Volume (mm <sup>3</sup> )
C11	9.9	9.5	76.98	1.9	731.31
C12	9.9	9.9	76.98	2.0	762.10
C13	9.8	10.0	75.43	2.1	754.30
C14	9.8	9.8	75.43	1.9	739.21
C15	9.8	10.0	75.43	2.0	754.30
C16	9.8	9.9	75.43	1.7	746.76
C21	23.7	24.2	441.15	24.0	10676
C22	23.7	24.2	441.15	24.0	10676
C23	23.7	24.2	441.15	23.5	10676
C24	23.7	24.6	441.15	24.3	10852
C25	23.7	24.4	441.15	23.5	10764
C26	23.7	23.9	441.15	23.9	10543
C31	44.9	45.3	1583.4	160.0	71728
C32	45.1	44.6	1597.5	160.0	71248
C33	45.1	45.1	1597.5	161.0	72047
C34	44.8	45.4	1576.3	159.0	71564
C35	45.0	45.3	1590.4	161.0	72045
C36	45.1	45.6	1597.5	161.5	72846
C41	99.5	100.3	7775.6	1795	779893
C42	99.6	100.2	7791.3	1770	780688
C43	99.5	100.6	7775.6	1790	782225
C44	99.5	100.5	7775.6	1805	781448
C51	192.2	192.9	29013	12585	5596608
C52	192.1	191.7	28983	12580	5556041
C53	192.2	193.6	29013	12645	5616917
C54	192.2	191.4	29013	12585	5553088

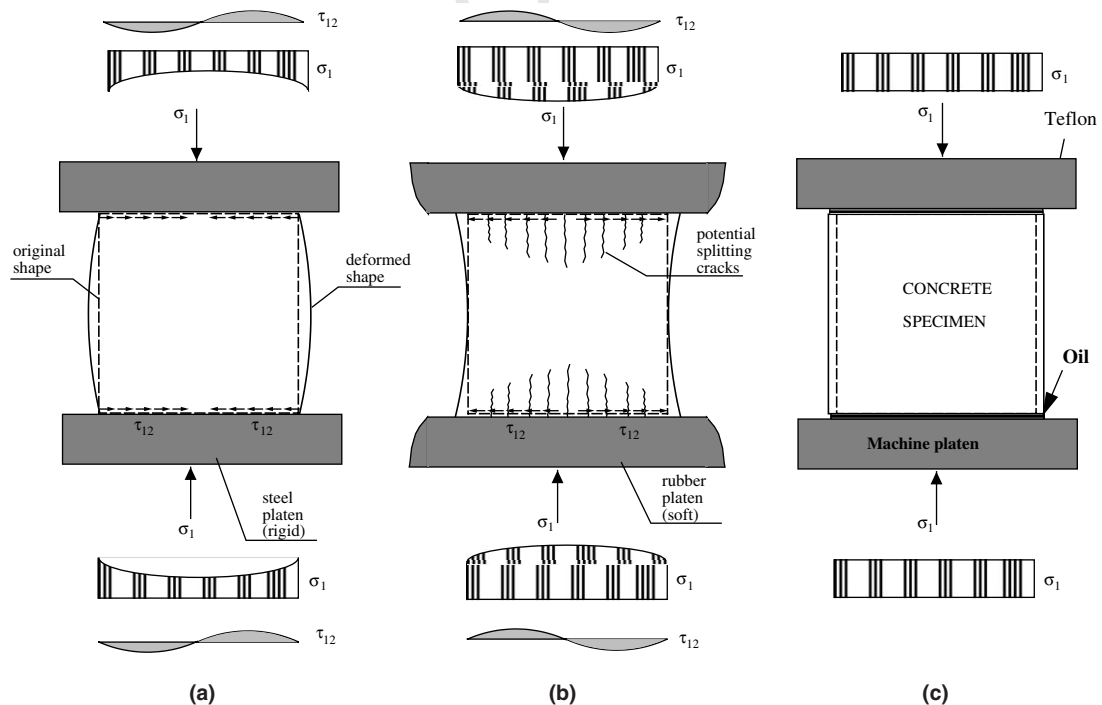


Fig. 2. Effect of loading platen response: (a) steel rigid platens; (b) soft platens and (c) adopted teflon layer proposed by van Vliet and van Mier [19].



The system adopted in the present compression tests comes from the analysis of the RILEM Technical Committee 148 SSC results [2]. The loading platens, they found, not only affect the post-peak behavior, but also the peak stress. Van Vliet and van Mier [13] observed an increase in peak stress by decreasing the slenderness (up to 200%), when the specimens were loaded between rigid steel platens, whereas an almost constant peak stress with the application of teflon interlayers. The softening branch, with both the systems, becomes steeper with increasing specimen height. These results suggested the use of two teflon layers of 150  $\mu\text{m}$  thickness with oil in between and a specimen slenderness equal to one.

### 3. Experimental observations

Only one representative curve for each of the five sizes has been selected, for graphical reasons. The summary of the experimental results for peak-load, stress at peak load and specific compressive energy is reported in Table 2. The experimental load versus displacement diagrams for smaller specimens ( $h = 10$  (C1), 23 (C2) and 46 mm (C3)) are reported in Fig. 3a, while those related to the larger specimens ( $h = 100$  (C4) and 190 mm (C5)) are reported in Fig. 3b. Moreover, a typical failure in the post-peak softening regime is shown in Fig. 4 (specimen C33).

#### 3.1. Stress–deformation response

The nominal stress versus nominal deformation curves are plotted in Fig. 5. These curves have been obtained from the load versus displacement curves by dividing the load by the initial specimen cross-section and the displacement by the initial specimen height. The curves show an initial steadily increasing slope, due to the lower stiffness at the beginning of the test. This fact is due to the adjustment of the loading platens to the specimen surfaces and to the compressibility of the teflon interlayers. This transition can be appreciated from Fig. 6, in which the axial and lateral strains obtained from strain gauges placed in the middle third of the specimen are plotted together with the axial strains obtained by dividing the piston-stroke by the specimen height. In the latter, the measured axial strains (called mean deformation,  $\epsilon_m$ , Fig. 6) also contain the deformation of the steel loading platens. This part is often substituted by a straight line with slope equal to the maximum pre-peak slope of the force–displacement curve. In this paper, the experimental curves have been presented as they have been recorded without any correction. Another possible correction that could be done on the experimen-

Table 2

Summary of experimental results for peak-load, stress at peak load and critical compressive energy density

Specimen no.	Peak load (daN)	Stress at peak load (N/mm <sup>2</sup> )	Stress–strain area (N/mm <sup>2</sup> )
C11	295	38.32	6.12
C12	328	42.61	7.32
C13	327	43.35	7.12
C14	335	44.41	8.34
C21	1289	29.22	2.51
C22	1457	33.03	3.45
C23	1229	27.86	2.75
C24	1404	31.83	2.78
C31	5298	33.46	1.33
C32	6136	38.41	2.90
C33	5813	36.39	2.62
C34	6311	40.04	3.24
C41	27247	35.04	0.32
C42	39194	50.30	0.33
C43	39231	50.45	0.20
C44	29923	38.48	0.42
C51	142400	49.08	–
C53	132210	45.57	0.35



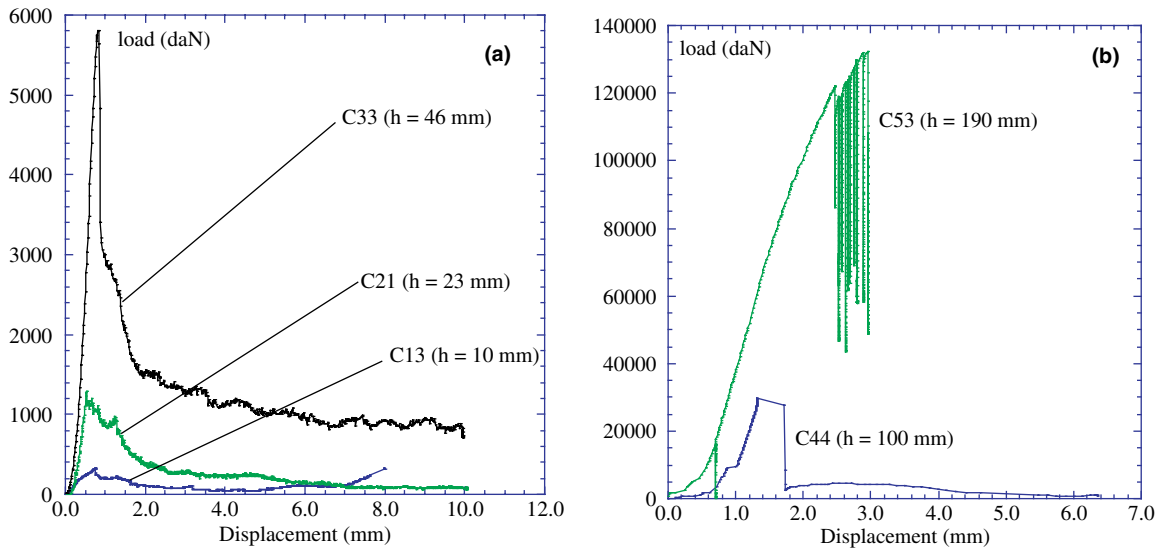


Fig. 3. Experimental load versus displacement curves: (a) small specimens,  $h = 10$  (C1), 23 (C2) and 46 mm (C3); (b) and large specimens,  $h = 100$  (C4) and 190 mm (C5).

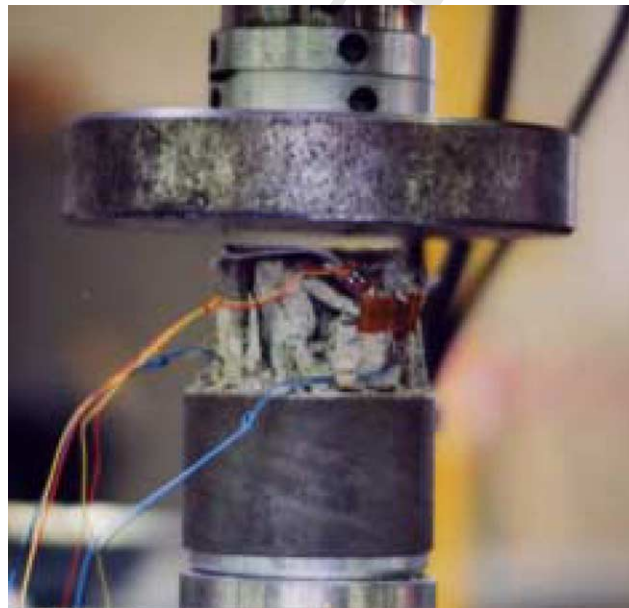


Fig. 4. Typical failure of a specimen in the post-peak softening regime.

tal curves is related to the different testing machine used for different specimen sizes. In this case, the two different experimentally evaluated stiffnesses for the set-ups, obtained with the teflon layers without any specimen, could be subtracted from the experimental diagrams.

After this initial part, the stress–strain path is nearly linear and this linear part is as more pronounced as the specimen is larger (Fig. 5). The smaller the specimen, the more pronounced pre-peak nonlinearities are. After the peak stress, a gradual descending branch has been detected. To appreciate the shape of the stress–strain curve better, its normalized version obtained by dividing the stresses by the peak stress (Fig. 7a) and the strains

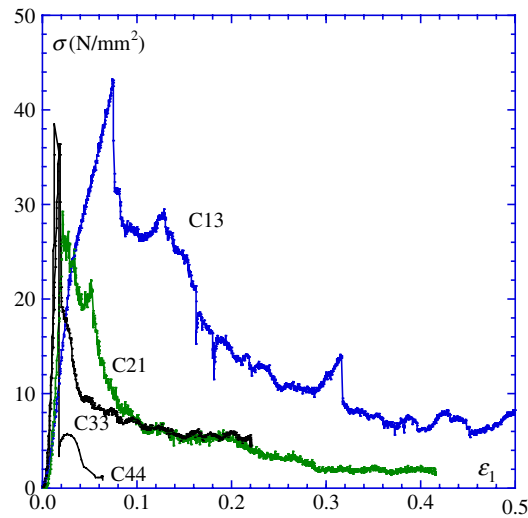


Fig. 5. Nominal stress versus nominal strain diagrams for four different cylindrical specimen sizes.

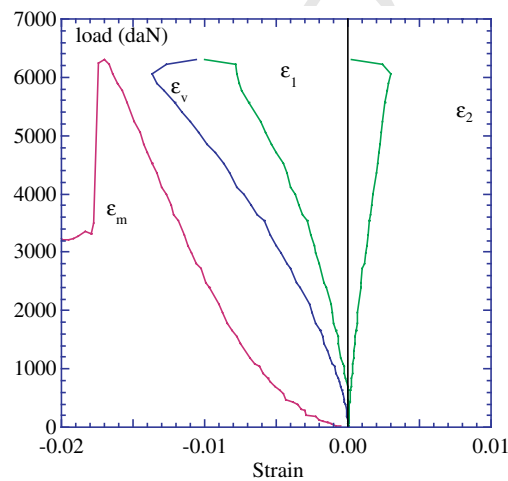


Fig. 6. Axial ( $\epsilon_1$ ), lateral ( $\epsilon_2$ ), volumetric ( $\epsilon_v$ ) and mean ( $\epsilon_m$ ) deformations for specimen C34.

187 by the strain at the peak stress (Fig. 7b) are reported. As can be deduced from Fig. 7, the stress–strain curve  
 188 for different specimens are almost the same in the pre-peak regime, but, beyond the peak, the slope of the post-  
 189 peak part decreases with decreasing specimen height. Van Mier [22] plotted the normalized stress versus post-  
 190 peak displacement curves, in which the displacements are calculated as

$$192 \quad \delta = (\epsilon - \epsilon_{\text{peak}})h \quad (1)$$

193 and obtained nearly overlapped curves. He concluded that, as the same displacement is needed to fracture the  
 194 specimens, the post-peak deformation must be localized in a small zone, and cannot be interpreted as an aver-  
 195 age strain. This fracture localization of concrete uniaxial compression implies that strain cannot be used as  
 196 state variable in constitutive laws. The dimensionless stress versus post-peak deformation diagrams for four  
 197 cylindrical specimen sizes are plotted in Fig. 8. It can be effectively observed that these curves are close to each  
 198 other, even if different initial slopes, indicating an increase in brittleness with size, is present.

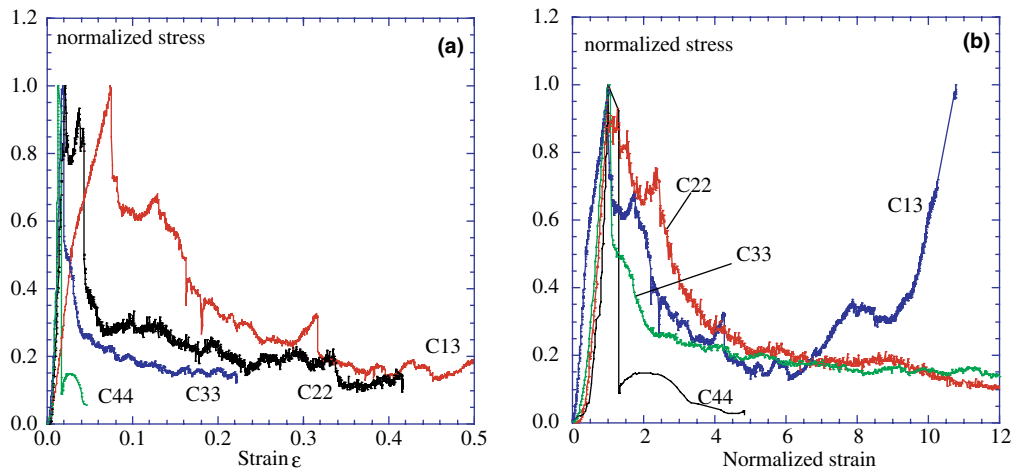


Fig. 7. (a) Normalized stress–strain diagrams for four different cylindrical specimen sizes; (b) normalized stress versus normalized strain diagrams for four different cylindrical specimen sizes.

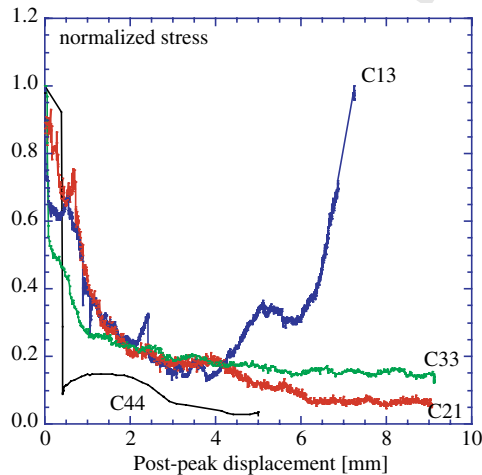


Fig. 8. Dimensionless stress versus post-peak displacement for four different cylindrical specimen sizes.

### 3.2. Scatter in peak stress

The values of the peak stresses, which are commonly called *compressive strength*, are reported in Fig. 9 by varying specimen sizes. It can be noticed how in compression a marked size effect does not come out and no relation with the specimen size is evident, as instead can be observed in tension [26–28] or in compression when localization is present [1]. The same results were obtained experimentally by the RILEM Committee 148 and numerically by Carpinteri et al. [29,30] by simulations with a boundary element approach. The scatter in the results is pronounced. What is interesting to observe is that the values even for the smallest size are comparable to the compressive strength of standard cubes. This permits us to affirm that, if friction is avoided or drastically reduced, the compressive strength of an existing concrete structure can be evaluated using very small drilling core specimens (nondestructive test method).

### 3.3. Scatter in dissipated energy density

The dissipated energy density can be evaluated by considering the area under the  $P$ – $\delta$  curve divided by the volume of the specimen. This is equivalent to considering the area under the stress–strain curve. For the small-

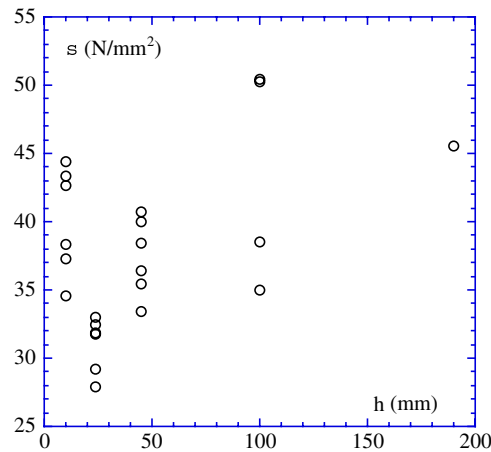


Fig. 9. Peak stresses by varying specimen size.

est specimen size, the dissipated energy density has been evaluated by considering the area under the stress–strain curve up to the minimum value of the stress. The numerical values of these areas for each specimen are reported in Table 2. The values are also plotted versus the characteristic specimen size in Fig. 15. This dissipated energy density undergoes severe scale effects, and the trend is a decrease by increasing the specimen dimension. This interesting result is discussed in the next section and a theoretical explanation is presented based on a fractal hypothesis for the fragment size distribution generated during the compression test.

#### 4. Full stress–strain curves

In this section the full stress–strain curves for the smallest cylindrical specimens ( $h = 10$  mm) are presented and some considerations are proposed. An interesting discussion of full stress–strain curve is proposed in the paper by Armer and Grimer [31]. They considered the re-ascending stress–strain branch which is not usually considered. This phenomenon was also described by Nikitin [32] by using dynamic analysis.

The complete curve for specimen C13 is plotted in Fig. 10. After the specimen has been crushed down more or less to a heap of aggregates, the resistance to further deformation reaches a minimum for  $\epsilon \simeq 0.5$ , and then begins to increase once more to higher stresses. Armer and Grimer affirm the existence of a new higher peak, at which the aggregate itself begins to break down. From the present experimental tests (Figs. 10 and 11) the author's opinion is that the re-ascending curve tends to an oblique asymptote rather than to a new peak. The increase of load will continue and when all the aggregates will be pulverized, the slope of the asymptote has to coincide with the test machine stiffness.

Physically, the valley zone BCD of the nominal stress versus average strain for the specimen C12 (Fig. 11) reflects the macroscale breakdown of the specimen and the following restructuring of the material into a new stable form.

The knowledge of the full load versus displacement (or nominal stress versus average strain) diagram can be very useful in a load-controlled experimental test. In this case, after the peak load (point B) a snap-through instability is evidenced, and a horizontal jump up to point D occurs. The energy under the curve BCD is released suddenly in a blasting way. Of course, point D corresponds to a new equilibrium configuration, which is usually not achievable, as the instantaneous release of energy is transformed into kinetic energy with expulsion of fragments. The curve, therefore, can be used to determine the specific energy released in the case of load-controlled test.

In concrete diamond drilling it can be observed how the snap-trough phenomenon just described can be very useful to simulate numerically the necessary energy (elastic and kinetic) to break concrete and to determine the chip size. For crushing phenomena (in concrete recycling, for example) it is very interesting to observe that the energy required to fragment a specimen (or in general a concrete element) is much larger than

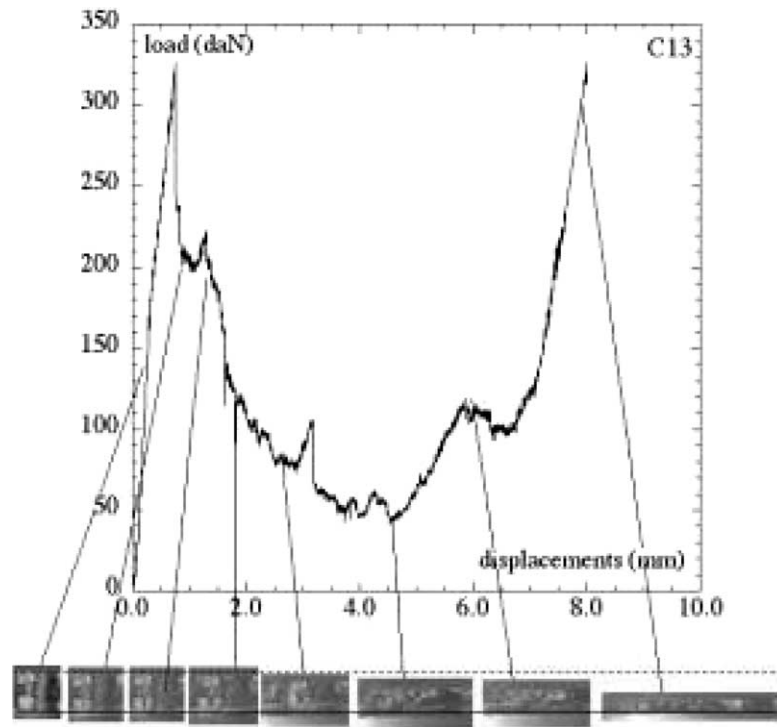


Fig. 10. Complete load versus displacement diagram up to compaction for the smallest specimen.

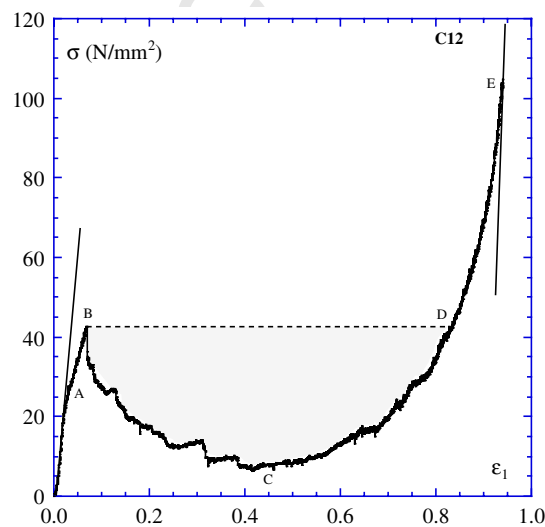


Fig. 11. Complete nominal stress versus nominal strain curve up to compaction for the smallest specimen size.

the elastic energy or the energy under the softening curve. This is due to the fact that the fragmentation and the formation of smaller chips is related to the surface area of the chips and this strongly increases by decreasing the size of the chips.

Finally, the last part of the curve can be influenced by the confinement due to the interaction of the aggregates with the machine platens. The interaction can be compared with the confinement effect due to the steel

reinforcement in building columns which undergo earthquakes. In this case, if the confinement is well designed, the evaluation of re-ascending curve for concrete can be very useful.

## 5. Fractal explanation of size effects on dissipated energy density in compression

The performed compression tests have shown an evident decrease of dissipated energy density with increasing specimen dimension (Fig. 15). This interesting phenomenon can be interpreted by considering the fragmentation and the comminution theories. In this field, fractal geometry represents a very helpful tool to explain such a phenomenon [16,17]. Turcotte [18] in the formulation of his fragmentation theory explains the difficulties in developing comprehensive theories. A primary reason is that fragmentation involves initiation and propagation of fractures. Fracture propagation is a highly nonlinear process requiring complex models even for the simplest configuration. Fragmentation involves the interaction between fractures over a wide range of scales. If fragments are produced over a wide range of sizes and if natural scales are not associated with either the fragmented material, fractal distribution of fragment number versus size would seem to be expected [33]. Let us consider a concrete specimen which undergoes a compression test. As is shown in Fig. 4, in the post-peak softening regime the specimen is characterized by the generation of a large number of fragments. After fragmentation, the number of fragments  $N$  with a characteristic linear dimension greater than  $r$  should satisfy the relation:

$$N = \frac{B}{r^D}, \quad (2)$$

where  $B$  is a constant of proportionality, and  $D$  is the fractal dimension.

In order to describe the mechanical meaning of the fractal exponent  $D$ , in Fig. 12 some examples of discrete fragmentation model are presented, where fragmentation is a scale-invariant process that leads to a fractal distribution of chip sizes. Let consider a fractal cube and use it as the basis for a fragmentation model. The fragmentation is such that some blocks are retained at each scale but others are fragmented. In Fig. 12a two diagonally opposed blocks are retained at each scale. For this configuration we have  $N_1 = 2$  for  $r_1 = \frac{h}{3}$ ,  $N_2 = 50$  for  $r_2 = \frac{h}{9}$ , and  $N_3 = 1250$  for  $r_3 = \frac{h}{27}$ . In order to determine  $D$ , Eq. (2) can be written as

$$D = \frac{\log(N_{n+1}/N_n)}{\log(r_n/r_{n+1})} \quad (3)$$

and then we can find for this case that  $D = \log 25 / \log 3 = 2.93$ . This is the fractal distribution of a discrete set. The cumulative number of blocks larger than a specified size for the three highest orders are  $N_{1c} = 2$  for  $r_1 = \frac{h}{3}$ ,  $N_{2c} = 52$  for  $r_2 = \frac{h}{9}$  and  $N_{3c} = 1302$  for  $r_3 = \frac{h}{27}$ , obtaining a value  $D = 2.95$ .

In Fig. 12b eight angular diagonally opposed blocks are retained at each scale. For this configuration we have  $N_1 = 8$  for  $r_1 = \frac{h}{3}$ ,  $N_2 = 152$  for  $r_2 = \frac{h}{9}$ , and  $N_3 = 2888$  for  $r_3 = \frac{h}{27}$ , so that  $D = \log 19 / \log 3 = 2.68$ . The cumulative number of blocks larger than a specified size for the three highest orders are  $N_{1c} = 8$  for  $r_1 = \frac{h}{3}$ ,  $N_{2c} = 160$  for  $r_2 = \frac{h}{9}$  and  $N_{3c} = 3048$  for  $r_3 = \frac{h}{27}$ , obtaining a value  $D = 2.70$ .

In Fig. 12c the limit case of localization is presented in which 18 angular blocks are retained at each scale, while only nine central blocks are fragmented. For this configuration we have  $N_1 = 18$  for  $r_1 = \frac{h}{3}$ ,  $N_2 = 162$  for  $r_2 = \frac{h}{9}$ , and  $N_3 = 1458$  for  $r_3 = \frac{h}{27}$ , so that  $D = \log 9 / \log 3 = 2.00$ . The cumulative number of blocks larger than a specified size for the three highest orders are  $N_{1c} = 18$  for  $r_1 = \frac{h}{3}$ ,  $N_{2c} = 180$  for  $r_2 = \frac{h}{9}$  and  $N_{3c} = 1638$  for  $r_3 = \frac{h}{27}$ , obtaining a value  $D = 2.05$ .

The same value for  $D$  can be obtained by retaining at each scale 18 blocks and fragmenting nine blocks placed this time in the configuration displayed in Fig. 12d. In this case,  $D = 2$ , but differently from Fig. 12c when we obtained a surface in correspondence of the central part of the largest block, we observe that the fragmentation phenomenon is localized in different small zones. Localization does not mean in this case dissipation on a surface (fracture or shear band), but rather localization of failure in concentrated zones.

The fractal dimensions for the discrete set and for the cumulative statistics are nearly equal. In Fig. 13 the cumulative statistics are reported for three fragmentation models.

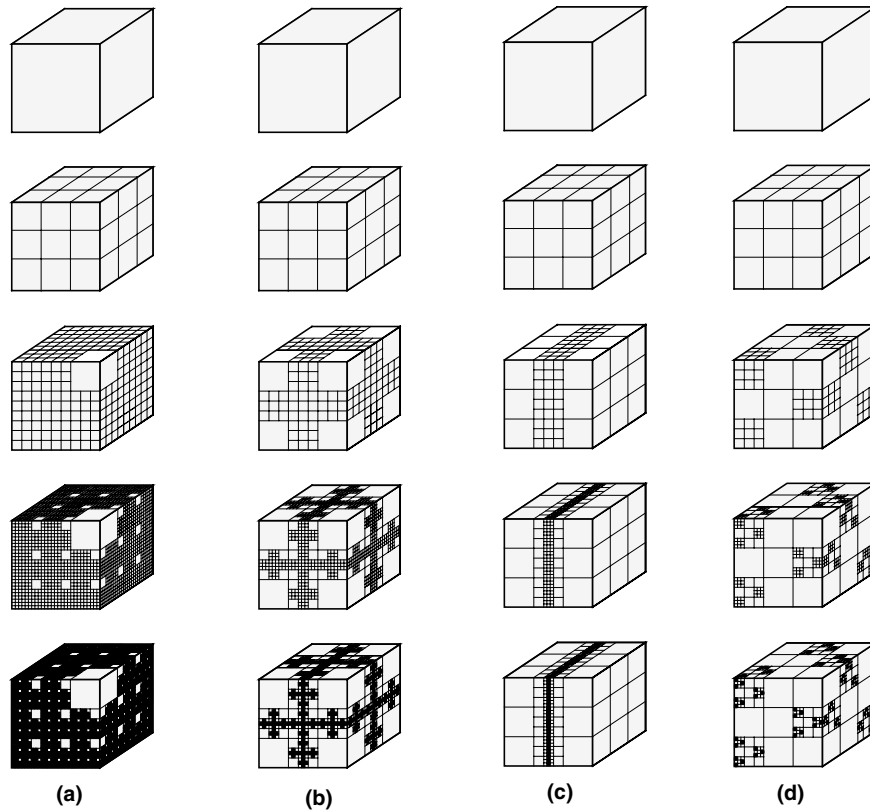


Fig. 12. Physical meaning of exponent  $D$ ; (a) at each step only one cube is retained, while all the others are divided into 27 equal-sized cubes with  $r_n = \frac{1}{3}r_{n-1}$  ( $D = 2.93$ ), very close to a volumetric fragmentation; (b) at each step the eight angular cubes are retained, while all the others 19 are divided into 27 equal-sized cubes with  $r_n = \frac{1}{3}r_{n-1}$  ( $D = 2.70$ ); (c) and (d) at each step the nine central cubes are divided into 27 equal-sized cubes with  $r_n = \frac{1}{3}r_{n-1}$ , while the others 18 are retained ( $D = 2.00$ ), showing a localization of the dissipation energy.

The total volume (mass) of fragments is given by [33]

$$V_f = \int_{r_{\min}}^{r_{\max}} r^3 dN, \quad (4)$$

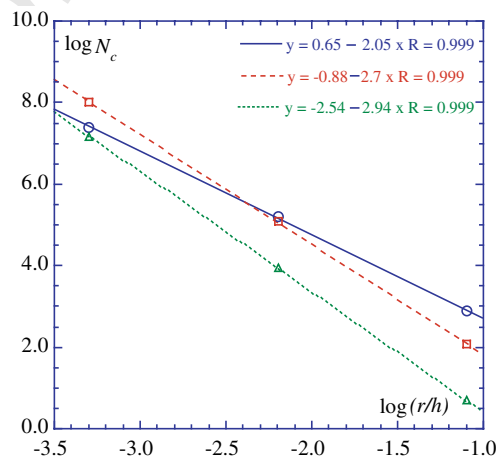


Fig. 13. Cumulative statistics for the fragmentation models proposed in Fig. 12.



since  $r$  has been defined to be the cube root of the fragment volume. It is expected that there will be upper and lower limits to the validity of the fractal (power-law) relation for fragmentation. The upper limit  $r_{\max}$  is generally controlled by the size of the fragmented object ( $r_{\max} = k\sqrt[3]{V}$  [34]). The lower limit  $r_{\min}$  is likely to be controlled by the scale of the heterogeneities responsible for fragmentation (grain size). For a power-law (monofractal hypothesis) distribution of sizes, substituting  $dN = -BD r^{(-D-1)} dr$ , with  $B$  a constant of integration, into Eq. (4) and integrating gives:

$$V_f = \frac{-DB}{3-D} (r_{\max}^{3-D} - r_{\min}^{3-D}), \quad (5)$$

where, for  $0 < D < 3$ , the specification of  $r_{\min}$  is not necessary. In this case the volume (mass) of fragments is predominantly provided by the largest fragments, so that  $V_f$  can be rewritten as

$$V_f = \frac{-DB}{3-D} r_{\max}^{3-D} \quad \text{for } 0 < D < 3, \quad (6)$$

and then

$$V_f = \frac{-DB}{3-D} k^{3-D} V^{1-\frac{D}{3}}. \quad (7)$$

On the other hand, the total surface area  $A_f$  of the fragments is given by

$$A_f = C \int_{r_{\min}}^{r_{\max}} r^2 dN, \quad (8)$$

where  $C$  is a geometrical factor depending upon the average shape of the fragments. For a power-law distribution, substitution of  $dN = -DB r^{-D-1} dr$  into Eq. (8) and integrating gives:

$$A_f = \frac{-DBC}{D-2} \left( \frac{1}{r_{\min}^{D-2}} - \frac{1}{r_{\max}^{D-2}} \right). \quad (9)$$

If  $0 < D < 2$ , it is necessary to specify  $r_{\max}$  in order to obtain a finite total surface area for fragments. If  $D > 2$ , it is necessary to specify  $r_{\min}$  in order to constrain the total surface area to a finite value. Usually the surface area of the smallest fragments dominates:

$$A_f = \frac{-BDC}{D-2} \frac{1}{r_{\min}^{D-2}}. \quad (10)$$

It can be assumed that the energy dissipated to produce a new free surface in the fragmentation process is provided by the product of specific energy absorbing capacity  $\beta_F$  and the total surface area  $A_f$ , for  $2 < D < 3$  [17]:

$$W = \beta_F A_f = \beta_F A_f \frac{V}{V} \quad (11)$$

in which  $\beta_F$  should have dimension of  $[F][L]^{(D-1)}$ . From Eq. (7),  $V$  can be expressed as

$$V = V^{D/3} V_f \frac{3-D}{-DB} k^{D-3} = \frac{r_{\max}^3}{k^3}. \quad (12)$$

In this case it is possible to have, from Eqs. (6) and (7):

$$W = \beta_F A_f \frac{V}{V} = \beta_F A_f \frac{V_f V^{D/3} \frac{3-D}{-DB} k^{D-3}}{\frac{r_{\max}^3}{k^3}} = \left( \beta_f \frac{-BCD}{D-2} r_{\min}^{2-D} r_{\max}^D k^D \right) V_f^{\frac{D}{3}} = \mathcal{G}_F^* V_f^{\frac{D}{3}}. \quad (13)$$

The two extreme cases contemplated by Eq. (13) are  $D = 2$ , surface theory [35,36], when the dissipation really occurs on a surface ( $W \propto V^{\frac{2}{3}}$ ) and by  $D = 3$ , volume theory [37], when the dissipation occurs in a volume ( $W \propto V$ ). In this case  $\mathcal{G}_F^*$  presents the following physical dimension:

$$[\mathcal{G}_F^*] = \left( \beta_f \frac{-BCD}{D-2} r_{\min}^{2-D} r_{\max}^D k^D \right) = [F][L]^{D-1} [L]^{2-D} [L]^{-D} = [F][L]^{1-D}. \quad (14)$$

For  $D = 2 \rightarrow [\mathcal{G}_F^*] = [F][L]^{-1}$ , which is the canonical dimension for fracture energy, while for  $D = 3 \rightarrow [\mathcal{G}_F^*] = [F][L]^{-2}$ , which is the physical dimension of stress. The experimental cases of fragmentation are usually intermediate ( $D \cong 2.5$ ) [18], as well as the size distribution for concrete aggregates due to Fuller [38].

If we consider  $V = h^3$ , we can write the expression of the dissipated energy density, from Eq. (13):

$$S = \frac{W}{V} = \mathcal{G}_F^* h^{D-3}. \quad (15)$$

The relationship of dissipated energy density related to different sizes can be posed in logarithmic form:

$$\log S = \log \mathcal{G}_F^* + (D - 3) \log h. \quad (16)$$

Eq. (16) represents a straight line with slope  $(D - 3)$  in the  $\log S$  versus  $\log h$  plane (Fig. 14). If  $D = 2$ , the slope is  $-1$ , as well as  $D = 3$  implies a vanishing slope.

The same results can be obtained in a different way, by considering a sequence of scales of observation [39]. Considering  $W$  as the global dissipated energy measured by the experimental set-up,  $\mathcal{G}$  as the elastic energy release rate or the specific energy necessary to generate the unit area of fracture, which is by hypothesis invariant with respect to the scale of observation, we have:

$$W = \mathcal{G}A, \quad (17)$$

and then:

$$\mathcal{G} = \frac{W}{A} = \frac{SV}{A} = \frac{Sh^3}{h^2} = Sh. \quad (18)$$

If we consider a sequence of scale of observation, we have:

$$\mathcal{G} = S_1 h_1 = \dots = S_{n-1} h_{n-1} = S_n h_n = S_{n+1} h_{n+1} = \dots = S_\infty h_\infty, \quad (19)$$

where the first scale of observation could be the macroscopic one, with  $S_1 h_1 = Sh$ ,  $h$  being the characteristic linear dimension of the specimen, and the asymptotic scale of observation could be the microscopic one, with  $S_\infty h_\infty = \mathcal{G}_F^* h^*$ ,  $h^*$  being the measure of the fractal set representing the fragmented configuration. It is important to underline that the measure  $h^*$  assumes finite value only for one particular value of  $d_\omega$  equal to the fractal dimension of the set (Hausdorff dimension). For any other values of  $d$ ,  $h^* = 0$  for  $d < d_\omega$  and  $h^* = +\infty$  for  $d > d_\omega$ . From the equality between the extreme members we can write:

$$S = \mathcal{G}_F^* \left( \frac{h^*}{h} \right), \quad (20)$$

or

$$S = \mathcal{G}_F^* \left( \frac{h^{1-d_\omega}}{h} \right), \quad (21)$$

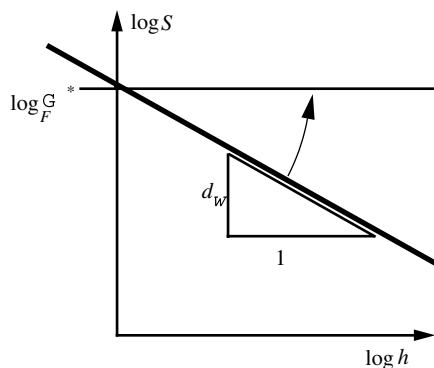


Fig. 14. Size effect on dissipated energy density in compression.

where  $0 < d_w < 1$  is the decrement of the topological dimension due to fragmentation. Taking the logarithms of both members of Eq. (21) we obtain:

$$\log S = \log \mathcal{G}_F^* - d_w \log h, \quad (22)$$

where  $d_w = 3 - D$  can be considered as the decrement of the topological dimension of the set in which energy dissipation occurs. When  $d_w = 1$  we obtain  $D = 2$  (localization); when  $d_w = 0$  we have  $D = 3$  (volumetric dissipation). Localization assumes here the meaning of dissipation localized in concentrated zones. Eq. (22) is identical to Eq. (16).

The values of dissipated energy density for the three smallest sizes are plotted in Fig. 15a against the specimen size in a bilogarithmic plane. The values for the four available sizes are instead reported in Fig. 15b. The size effect is represented by the slope of the linear regression of the points of the diagram. It is evident how the dissipated energy density decreases with increasing specimen size.

As may be seen from Fig. 15, the slope of the dissipated energy density decrease proves to be equal to 0.67 when only three specimen sizes are considered, and to 0.97 when considering the fourth size. We have considered the two different cases as the fourth size has been tested with a different procedure which can cause variations in energy estimation. In the former case, the physical meaning reveals an energy dissipation on a fractal space of dimension 2.33, while in the latter case the dissipation occurs on a fractal space of dimension 2.03, i.e., very close to a two-dimensional surface. In the second case, as the fractal space is close to a two-dimensional surface, different interpretations, by using the classical euclidean geometry, could be also proposed. In this approach, however, the fractal approach has been chosen. It is therefore possible to obtain a constant (universal) dissipated energy density equal to  $31 \text{ N mm}^{-1.33}$  and to  $74 \text{ N mm}^{-1.03}$ , respectively (Fig. 16). The graphic interpretation of the renormalization procedure is given in Fig. 14. The assumption of a fractal (or anomalous) physical dimension allows the determination of the dissipated energy density parameter  $\mathcal{G}_F^*$ , which results in independence of the scale. As it is easy to observe, in the latter case the renormalized dissipated energy density tends to be a fracture energy, the dissipation occurring on a fractal set very close to a two-dimensional surface. Such a result confirms the localization of the dissipation on a surface [25]. The fractal nature of the fragments generated by the compressive test emerges very clearly at the size scale of the specimens. Momber [10] applied fragmentation theory to the study of compression and analyzed the fragments, determining a fractal exponent  $D$  close to 2. On the other hand, the property of self-similarity is very likely to vanish or change at higher or lower scales, owing to the limited character of the particle size curve. The price to pay for obtaining a constant value is the loss of the classical physical dimensions for dissipated energy density. It is obviously very difficult to use these results in a structural analysis, a noneuclidean (or fractal) mechanics being not yet available, even if very important steps have been moved forward by Carpinteri et al. [40].

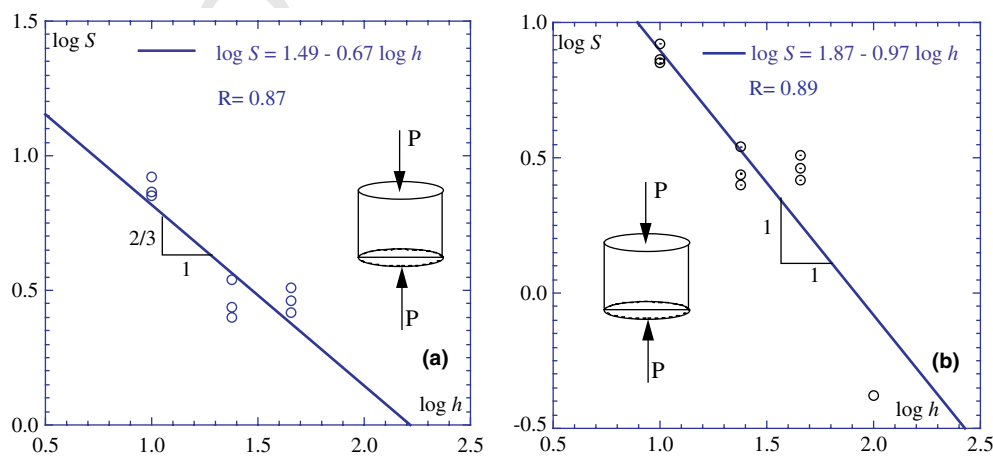


Fig. 15. Size effect on dissipated energy density (experimental tests).

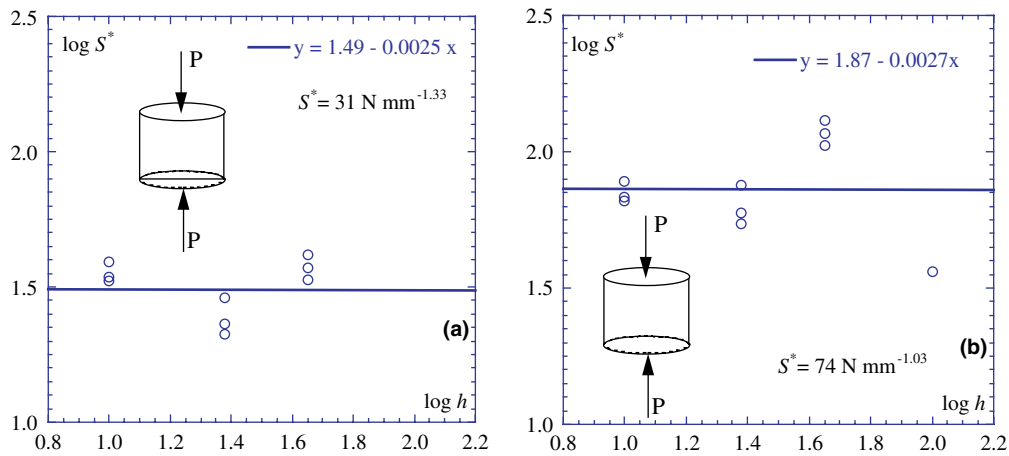


Fig. 16. Renormalized value of dissipated energy density (experimental tests).

## 6. Scale-independent constitutive law for concrete in compression

The experimental curves  $\sigma$  versus  $\epsilon$ , reported in Fig. 5, show a marked scale dependence, in particular for what concerns the post-peak part. These curves  $\sigma$  versus  $\epsilon$ , or  $F$  versus  $\delta$ , are in fact characterized by two different regimes. The first regime corresponds to the pre-peak elastic behavior, when microcracks form randomly in the specimen. At this stage the external force linearly increases until it reaches the peak value and the statistical fluctuations are very small. In the second regime, which could be called “catastrophic”, the interactions between the microcracks begin to rule the process, until macrofractures form and propagate through the whole specimen. In large specimens this phenomenon could occur with a sudden release of stored elastic energy.

In this section, a renormalization procedure is proposed to obtain a unique constitutive relationship for softening in compression. By assuming damage occurring in a fractal sub-domain inside the specimen, energy dissipation becomes scale-dependent. Hence it should be substituted by a fractal quantity, which is the true material constant. The assumption that the energy dissipation occurs in a sub-domain characterized by a fractal dimension, imposes the definition of fractal strain (or dilatation).

Let us consider the external work  $W$ , which presents the physical dimension of  $[F][L]$ . The nominal dissipated energy density,  $S = W/V$ , is usually the dissipated energy over the specimen volume, so that it presents the physical dimension of  $[F][L]^{-2}$  and can be evaluated by integration:

$$S = \frac{W}{V} = \int_0^{\epsilon_{\max}} \sigma(\epsilon) d\epsilon, \quad (23)$$

which represents the area under the  $\sigma$ – $\epsilon$  curve. Supposing that the energy dissipation does not occur in the specimen volume ( $V \propto l^3$ ) but in a fractal domain of dimension  $D$  ( $V \propto l^D$ ), and considering  $[\sigma] = [F][L]^{-2}$  as the nominal stress, in order to obtain a constant specific compression energy, the strain has to assume a physical dimension of  $[L]^{-(D-3)} = [L]^{d_w}$  [40,41]. In fact, in this hypothesis, if  $W$  is dissipated over a domain with physical dimension of  $[L]^D$ , we obtain:

$$[S] = \frac{[W]}{[V]} = \frac{[F][L]}{[L]^D} = [F][L]^{1-D}. \quad (24)$$

For  $D = 2$  (surface theory, dissipation occurring on a surface)  $\rightarrow S = [F][L]^{-1}$ , while for  $D = 3$  (volume theory, dissipation occurring on a volume)  $\rightarrow S = [F][L]^{-2}$ . Assuming to maintain the nominal stress  $\sigma$  with physical dimension of  $[F][L]^{-2}$ , from Eq. (23) we have:

$$[S] = [\sigma][\epsilon^*] = [F][L]^{-2}[L]^x = [F][L]^{1-D}, \quad (25)$$

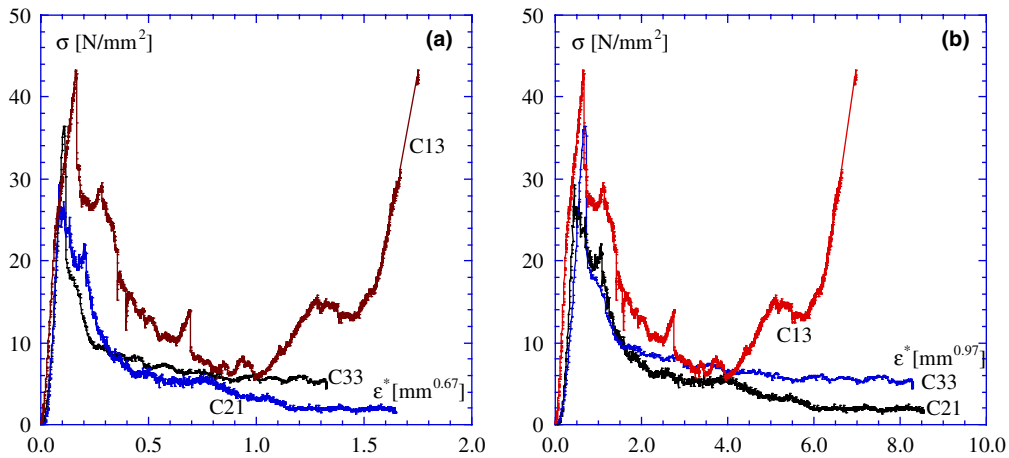


Fig. 17. Stress versus renormalized strain for three different specimen sizes: (a)  $D = 2.33$ ; (b)  $D = 2.03$ .

and than:

$$x = 3 - D = d_\omega. \quad (26)$$

In the monofractal hypothesis, the renormalized strain therefore assumes the physical dimension of  $[L]^{3-D}$ , defined as the displacements  $\delta$  divided by  $l = [L]^{D-2}$ .

By considering the fractal strain, a scale-invariant constitutive relationship can be obtained. In other words, the experimental diagrams related to the different sizes can be rescaled by considering the strain renormalization, and a clear superposition of the curves is evidenced. In Fig. 17a the strains are renormalized for  $D = 2.67$  as obtained from the fitting that considers only three sizes, while in Fig. 17b the dimension  $D = 2.03$  has been used. It is possible to observe how the curves tend to superpose one on each other and in particular how the variation in structural behavior disappears.

Lastly, from Fig. 17a and b, it can be observed how a renormalization (or a new definition) of the elastic modulus comes out. In fact, the elastic modulus is defined, from the classical Hooke law's, as the ratio between the stress and the strain. In the present analysis we obtain:

$$[E^*] = \frac{[\sigma]}{[\epsilon^*]} = \frac{[F][L]^{-2}}{[L]^{-(D-3)}} = [F][L]^{D-5}, \quad (27)$$

and in the two limit cases for  $D = 2$  (surface theory, dissipation occurring on a surface)  $\rightarrow E = [F][L]^{-3}$ , and assumes the physical dimension of a density, while for  $D = 3$  (volume theory, dissipation occurring on a volume)  $\rightarrow E = [F][L]^{-2}$  and we obtain the classical elastic modulus.

The renormalization previously presented is in good agreement with the methodology proposed by van Mier [42] in order to obtain a unique empirical stress–displacement relationship and applied to the present experimental curves (Fig. 8). In fact, in our results (Fig. 17) the renormalization strain has a physical dimension equal to 0.97, very close to 1, and then very close to a displacement. What is important to emphasize at this stage is that in compression we have dissipation of the energy over an area at small scales, while at large scales the energy dissipation occurs in a volume. This appears very interesting as it is the opposite trend with respect to tension, in which localization is evident for large specimens and not at small scales. Eventually, the renormalization procedure for large specimens ( $D = 3$ ) tends again to a stress–strain diagram, as  $\epsilon^* = \epsilon$ .

## 7. Conclusions

Uniaxial compression tests were performed under displacement control on drilled cylindrical specimens obtained from a single concrete block over a very large scale range (1:19), the largest range available in the literature. The friction between specimen ends and testing machine platens was reduced by using two layers

of teflon with oil in between. The experimental results show how, reducing the friction at the ends, the nominal compressive strength is not clearly affected by scale effects as is evident in tension. The tests performed on very small specimen sizes (10 mm diameter) and the independence of the dimension for the compressive strength allows us deep considerations for evaluating the effective strength of real concrete structures, that undergo deterioration of the mechanical properties and represent a dramatic problem in civil engineering. The results can be considered as a starting point in order to reconsider the standard dimension for evaluating the compressive strength of high-strength concretes, using the same testing machines available in the laboratories.

In addition, the full stress–strain curve in compression has been determined, and from those results it can be evidenced a snap-through instability allowing to quantify the energy required for fragmentation. The determination of the full curve is also important in concrete recycling industry to quantify the energy necessary for destroying concrete structures, even in blasting.

Finally, a theoretical explanation for the size effect on the dissipated energy density has been proposed, from which it appears how the dissipation occurs in a fractal sub-space of dimension comprised between a surface and a volume. A renormalization procedure for determining a constant dissipated energy density is also proposed and it comes out that, in the range of the tested specimens, the energy dissipation occurs in a fractal space very close to a two-dimensional surface. This is in a good agreement with the hypothesis proposed by van Mier [22] and by Lee and Willam [25], which stated that energy dissipation in the post-peak regime is a localized surface-dominated fracture process, after the coalescence of microcracks in the peak regime. This hypothesis is however valid only when small specimen sizes are used, whereas for large specimen sizes a volumetric dissipation occurs, as proposed by Carpinteri and Ferro [43] in a forthcoming paper.

## Acknowledgements

The present research was carried out with the financial support of the Ministry of University and Scientific Research (MIUR) under the grant PRIN 2003 “Damage mechanics and durability of ordinary and high performance concrete”. The author is thankful to Mr. Vincenzo Angilletta for his technical support in performing the experimental tests.

## References

- [1] Carpinteri A, Ferro G, Monetto I. Scale effects in uniaxially compressed concrete specimens. *Mag Concr Res* 1999;51:217–25.
- [2] Karihaloo BL, Lange-Kornback D. Strain-softening of concrete in uniaxial compression. *Mater Struct* 1997;30:195–209 (R. of the round robin test carried out by RILEM TC 148-SSC).
- [3] Gonnermann H. Effect of size and shape of test specimen on compressive strength of concrete. *Proc ASTM* 1925;25:237–50.
- [4] Blanks R, McNamara C. Mass concrete tests in large cylinders. *J Am Concr Inst* 1935;31:280–303.
- [5] Jishan X, Xixi H. Size effect on the strength of a concrete member. *Engng Fract Mech* 1990;35:687–95.
- [6] Barr B, Abusiaf H, Sener S. Size effect and fracture energy studies using compact compression specimens. *Mech Mater* 1998;31:36–41.
- [7] Bažant Z, Kwon Y. Failure of slender and stocky reinforced concrete columns: tests and size effects. *Mater Struct* 1994;27:79–90.
- [8] Campione G, Mindess S. Size effect in compression of high strength fibre reinforced concrete cylinders subjected to concentric and eccentric loads. In: Banthia N, editor. *ACI special publication on fibre reinforced concrete*. 2001. p. 86–91.
- [9] Carpinteri A, Chiaia B, Ferro G. Multifractal scaling law: an extensive application to nominal strength size effect of concrete structures. Technical Report 51, *Atti del Dipartimento di Ingegneria Strutturale del Politecnico di Torino*, 1995.
- [10] Momber A. The fragmentation of standard concrete cylinders under compression: the role of secondary fracture debris. *Engng Fract Mech* 2000;67:445–59.
- [11] Slate FO, Hover KC. Microcracking in concrete. In: Carpinteri A, Ingrassia R, editors. *Fracture mechanics of concrete*. The Hague: Martinus Nijhoff Publishers; 1984. p. 137–59.
- [12] Vardoulakis I, Labuz JF, Papamichos E, Tronvoll J. Continuum fracture mechanics of uniaxial compression on brittle materials. *Int J Solids Struct* 1998;35:4313–35.
- [13] van Vliet M, van Mier J. Experimental investigation of concrete fracture under uniaxial compression. *Mech Cohesive-Frict Mater* 1996;1:115–27.
- [14] Carpinteri A, Pugno N. A fractal comminution approach to evaluate the drilling energy dissipation. *Int J Numer Anal Methods Geomech* 2002;26:499–513.
- [15] Carpinteri A, Pugno N. One-, two- and three-dimensional universal laws for fragmentation due to impact and explosion. *J Appl Mech* 2002;69:854–6.
- [16] Mandelbrot BB. *The fractal geometry of nature*. New York: W.H. Freeman and Company; 1982.
- [17] Borodich FM. Fractals and fractal scaling in fracture mechanics. *Int J Fract* 1999;95:239–59.

- [18] Turcotte DL. Fractals and fragmentation. *J Geophys Res* 1986;91:1921–6.
- [19] van Vliet M, van Mier J. Softening behaviour of concrete under uniaxial compression. In: Wittmann F, editor. *Fracture mechanics of concrete structures*. AEDIFICATIO Publishers; 1995. p. 383–96.
- [20] Jansen D, Shah S. Effect of length on compressive strain softening of concrete. *J Eng Mech (ASCE)* 1997;123:25–35.
- [21] Kotsovos MD. Effect of testing techniques on the post-ultimate behavior of concrete in compression. *Mech Mater* 1989;16:1–12.
- [22] van Mier J. Multiaxial strain-softening of concrete – part i: fracture and part ii: load-histories. *Mater Struct* 1986;19:179–200.
- [23] Vonk RA. Softening of concrete loaded in compression. Ph.D. thesis, Eindhoven University of Technology, The Netherlands, 1992.
- [24] Wittmann F, Slowik V, Alvaredo A. Probabilistic aspects of fracture energy of concrete. *Mater Struct* 1994;27:499–504.
- [25] Lee Y-H, Willam K. Mechanical properties of concrete in uniaxial compression. *ACI Mater J* 1997;94:457–71.
- [26] Ferro G. Effetti di scala sulla resistenza a trazione dei materiali. Ph.D. thesis, Politecnico di Torino, 1994.
- [27] Carpinteri A, Ferro G. Size effects on tensile fracture properties: a unified explanation based on disorder and fractality of concrete microstructure. *Mater Struct* 1994;27:563–71.
- [28] Carpinteri A, Ferro G. Scaling behaviour and dual renormalization of experimental tensile softening responses. *Mater Struct* 1998;31:303–9.
- [29] Carpinteri A, Ciola F, Pugno N. Boundary element method for the strain-softening response of quasi-brittle materials in compression. *Comput Struct* 2001;51:389–401.
- [30] Carpinteri A, Ciola F, Pugno N, Ferrara MGG. Size-scale and slenderness influence on the compressive strain-softening behaviour of concrete. *Int J Fract Fatigue Engng Mater Struct* 2001;24:441–50.
- [31] Armer G, Grimer F. On the use of the full stress–strain characteristics in structural analysis. *Mater Struct* 1989;22:48–52.
- [32] Nikitin L. Failure of structures due to crack growth and damage. *Struct Safe* 1993;12:123–8.
- [33] Turcotte DL. *Fractals and chaos in geology and geophysics*. Cambridge University Press; 1992.
- [34] Carpinteri A. Mechanical damage and crack growth in concrete: plastic collapse to brittle fracture. Dordrecht: Martinus Nijhoff Publishers; 1986.
- [35] Rittinger PR. *Lehrbuch der aufbereitungskunde*, Berlin, 1937.
- [36] Hönig F. *Grundgesetze der zerkleinerung*. Technical Report 378, VDI Forschungsheft, 1936.
- [37] Kick F. *Das gesetz der proportionalen widerstande*, Leipzig, 1885.
- [38] Stroeve P. Fractals and fractography in concrete technology. In: *International symposium on brittle matrix composites*, Warsaw, Poland, 1991. p. 1–10.
- [39] Goldshtein R, Mosolov A. Fractal cracks. *J Appl Math Mech* 1992;56:563–71.
- [40] Carpinteri A, Cornetti P. A fractional calculus approach to the description of stress and strain localization in fractal media. *Chaos Solitons Fract* 2002;13:85–94.
- [41] Carpinteri A, Chiaia B, Cornetti P. A scale-invariant cohesive crack model for quasi-brittle materials. *Engng Fract Mech* 2002;69:207–17.
- [42] van Mier J. *Fracture process of concrete*. Boca Raton, FL: CRC Press; 1996.
- [43] Carpinteri A, Ferro G. Effects of specimen size on the dissipated energy density in compression, *Mech Mater*, submitted for publication.